AIAA JOURNAL
Vol. 40, No. 6, June 2002

Determining Aerodynamic Loads Based on Optical Deformation Measurements

Tianshu Liu,* D. A. Barrows,† A. W. Burner,‡ and R. D. Rhew*
NASA Langley Research Center, Hampton, Virginia 23681-2199

A preliminary study is described for determining aerodynamic loads based on optical elastic deformation measurements using a videogrammetric system. Data reduction methods are developed and used to extract the normal force and pitching moment from beam deformation data. The axial force is obtained by measuring the axial translational motion of a movable shaft in a spring/bearing device. Proof-of-concept calibration experiments are conducted to assess the feasibility of the optical technique for measuring aerodynamic loads. The uncertainties in optical force and moment measurements are discussed.

I. Introduction

INTERNAL strain gauge balances have been used for years as a standard technique for measuring the integrated aerodynamic forces and moments on models in wind tunnels. A variety of internal strain gauge balances have been developed, and the technical aspects of various balances have been studied in detail.[1] Generally speaking, the structure of an internal strain gauge balance is complicated, and the cost of fabrication is high. This paper presents an exploratory study for remotely measuring aerodynamic loads using a videogrammetic system. Unlike strain gauges, this method optically measures beam deformation to determine the normal force and pitching moment. The axial force is obtained by measuring the translational motion of a movable shaft in a spring/bearing device. Mathematical models for data reduction are developed to extract the aerodynamic forces and moments from the deformation data. Uncertainty analysis is given to evaluate the contributions from the elemental error sources and correlation terms. At this stage, the normal force, pitching moment, and axial force are the primary quantities to be determined. In principle, the side force, rolling moment, and yawing moment can be determined in a similar manner. Proof-of-concept laboratory experiments have been conducted to validate the proposed methodology for measuring the aerodynamic loads. Potentially, this optical method can be used as an alternative to strain gauge balances. In addition, the technique described in this paper can be integrated with optical model attitude and deformation measurement techniques.[2,3]

II. Cantilever Beam Deformation

The deformation of a cantilever beam is utilized in this study to calculate the normal force and pitching moment. Consider a cantilever beam bent by a force F and a moment M applied at the end, as shown in Fig. 1. According to the engineering beam theory in which the deformation due to shear strain is assumed to be negligible,[4] the normal coordinate v of the beam is described by

$$EI(x)v_{xx} = -F(L-x) - M \tag{1}$$

where v_{xx} is the second derivative with respect to x, M is the local bending moment, E is the modulus of elasticity, and $I(x)$ is the moment of inertia. The boundary conditions are $v_x(x=0) = v_{x0}$ and $v(x=0) = v_0$. The solution for the displacement $\delta v = v - v_0 - v_{x0}x$ is

$$\delta v(x) = -E^{-1}(FL+M)Q_1(x) + E^{-1}FQ_2(x) \tag{2}$$

where $Q_1(x)$ and $Q_2(x)$ are the coefficients defined as

$$Q_1(x) = \int_0^x \mathrm{d}x' \int_0^{x'} [I(x'')]^{-1}\,\mathrm{d}x''$$

$$Q_2(x) = \int_0^x \mathrm{d}x' \int_0^{x'} [I(x'')]^{-1}x''\,\mathrm{d}x''$$

For a rectangular cross section beam, the moment of inertia is $I = wh^3/12$, where w is the width and h is the height of the cross section. For a circular cross section beam, the moment of inertia is $I = \pi R^4/4$, where R is the radius of the circular cross section. When a beam has a constant cross section and the moment of inertia is constant, expression (2) becomes

$$\delta v(x) = -(EI)^{-1}(FL+M)x^2/2 + (EI)^{-1}Fx^3/6 \tag{3}$$

Therefore, the local displacement δv and the slope change $\delta v_x = v_x - v_{x0}$ are

$$\begin{pmatrix}\delta v\\ \delta v_x\end{pmatrix} = \begin{pmatrix}x^3/6EI & -x^2/2EI\\ x^2/2EI & -x/EI\end{pmatrix}\begin{pmatrix}F\\ M_c\end{pmatrix} \tag{4}$$

where $M_c = FL + M$ is the moment with respect to a moment center c. Equation (4) gives a linear relation between the deformation δv and δv_x and the force and moment F and M_c. When the deformation due to shear strain is taken into account, a more complete analysis of a rectangular cantilever beam gives a nonlinear relation between δv and δv_x and F and M_c (Ref. 5). The theoretical results provide basic models for data reduction to recover the force and moment. Generally, given the force and moment, the theoretical relations describe beam deformation profiles well. However, inversion to the force and moment from deformation measurements is a stiff problem that is very sensitive to small errors. In practical data reduction procedures, the theoretical results are combined with empiricism to deal with imperfections in the real measurements.

III. Data Reduction Methods

A. Method Based on Local Displacement and Slope

Equations (3) and (4) indicate that the force F and moment M_c depend on the local displacement δv and the change of slope δv_x. Therefore, F and M_c can be determined from measurements of δv and δv_x. Here, the pitching moment M_c is defined as $M_c = F(L - L_c)$, where L is the distance between the force (load) location and the beam support and L_c is the distance between the

Presented as Paper 2001-0560 at the AIAA 39th Aerospace Sciences Meeting, Reno, NV, 8–11 January 2001; received 15 February 2001; revision received 5 September 2001; accepted for publication 19 October 2001.

*Research Scientist, Model Systems Branch. Member AIAA.
†Engineer, Instrumentation Systems Development Branch.
‡Research Scientist, Instrumentation Systems Development Branch. Senior Member AIAA.

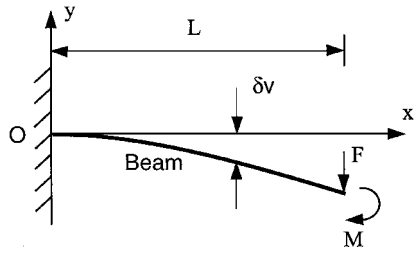

Fig. 1 Cantilever beam deformed by a force F and a moment M.

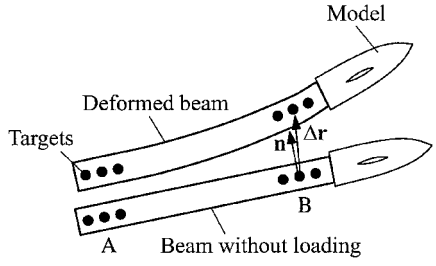

Fig. 2 Deformation of a beam (sting) with targets.

moment center c and the support. The local displacement and the change of slope are defined as

$$\delta v = v(x) - v(x_{\text{ref}}) - v_x(x_{\text{ref}})x_{\text{ref}}, \qquad \delta v_x = v_x(x) - v_x(x_{\text{ref}}) \tag{5}$$

where x_{ref} is the reference location where deformation is much smaller, such as a position near the support. Instead of directly using Eq. (5), the practical procedures for calculating δv and δv_x are based on a conformal transformation because of its robustness.

The quantities δv and δv_x are calculated from the optically measured coordinates of high-contrast targets positioned on the beam. Figure 2 shows a typical layout of targets on a beam (sting) connected with a wind-tunnel model. A row of targets, B in Fig. 2, is placed in parallel to the beam centerline near the wind-tunnel model. Another row of targets, reference targets A, is placed near the support of the beam. When the beam is deflected by aerodynamic loads, not only do the targets at B move, but also the reference targets at A may move slightly because the support is not absolutely rigid. Thus, the total movement of target row B contains both the relative deformation at B with respect to A and the local movement at A. The local deformation at B, which is more sensitive to loads, can be obtained by removing the local movement at A from the total movement at B.

To correct the movement of the reference target row A due to loads, the load-off (or wind-off) position of the target row A is used as a baseline position. Assuming that the local movement of the reference target row A can be approximated as rigid-body motion, one obtains a conformal transformation between the load-off coordinate $(\tilde{X}, \tilde{Z})$ and load-on coordinate (X, Z) for the reference target row A:

$$\begin{pmatrix} \tilde{X} \\ \tilde{Z} \end{pmatrix} = \begin{pmatrix} \cos\theta_A & \sin\theta_A \\ -\sin\theta_A & \cos\theta_A \end{pmatrix} \begin{pmatrix} X \\ Z \end{pmatrix} + \begin{pmatrix} T_{xA} \\ T_{zA} \end{pmatrix} \tag{6}$$

where θ_A is a rotational angle at A and T_{xA} and T_{zA} are the translations at A. The coordinate system (X, Y, Z) is a standard wind-tunnel coordinate system in which X is in the freestream flow direction, Y is in the spanwise direction, and Z is in the vertical direction. The beam deformation is in the (X, Z) plane. The rotational angle θ_A and the translations T_{xA} and T_{zA} can be determined from the measured load-off and load-on coordinates of target row A by using the least-squares method.

Applying the conformal transformation (6) to the load-on coordinates of the target row B, we are able to eliminate the effect of the local movement at A. We denote the transformed load-on coordinates of target row B as $\tilde{X}_{B\,\text{on}}$ and $\tilde{Z}_{B\,\text{on}}$ and call them the realigned load-on coordinates of target row B relative to the reference load-off target row A. The realigned load-on coordinates $\tilde{X}_{B\,\text{on}}$ and $\tilde{Z}_{B\,\text{on}}$ of the target row B are related to the corresponding load-off coordinates $\tilde{X}_{B\,\text{off}}$ and $\tilde{Z}_{B\,\text{off}}$ by the following conformal transformation:

$$\begin{pmatrix} \tilde{X}_{B\,\text{on}} \\ \tilde{Z}_{B\,\text{on}} \end{pmatrix} = \begin{pmatrix} \cos\theta_B & \sin\theta_B \\ -\sin\theta_B & \cos\theta_B \end{pmatrix} \begin{pmatrix} \tilde{X}_{B\,\text{off}} \\ \tilde{Z}_{B\,\text{off}} \end{pmatrix} + \begin{pmatrix} T_{xB} \\ T_{zB} \end{pmatrix} \tag{7}$$

The change of the bending angle at the target row B is θ_B, and $\Delta \boldsymbol{r}_B = (T_{xB}, T_{zB})$ is the displacement vector at the target row B. The values of θ_B and $\Delta \boldsymbol{r}_B = (T_{xB}, T_{zB})$ can be determined by using the least-squares method, representing the average quantities of local deformation for the target row B. Therefore, the normal displacement and the change of the slope at B due to loads are, respectively,

$$\delta v = \boldsymbol{n}_B \cdot \Delta \boldsymbol{r}_B, \qquad \delta v_x = \tan(\theta_B) \tag{8}$$

where $\boldsymbol{n}_B$ is the unit vector normal to the beam axis at B.

In reality, the relationship between F and M_c and δv and δv_x is more complicated than theoretical prediction by the engineering beam theory. The relations for calculating F and M_c are generally expressed as

$$F = f_1(\delta v, \delta v_x), \qquad M_c = f_2(\delta v, \delta v_x) \tag{9}$$

In practice, we do not tend to fit globally the whole set of calibration data to obtain the complete functional relations. Instead, for a given data point $(\delta v, \delta v_x)$, we use a local second-order polynomial to interpolate a group of neighboring calibration data points, that is,

$$F = \boldsymbol{B}_1 \boldsymbol{\delta}, \qquad M_c = \boldsymbol{B}_2 \boldsymbol{\delta} \tag{10}$$

where $\boldsymbol{\delta} = [\delta v, \delta v_x, (\delta v)^2, \delta v \delta v_x, (\delta v_x)^2]^T$ is the deformation vector and $\boldsymbol{B}_1$ and $\boldsymbol{B}_2$ are the coefficients determined by calibration.

A simple model approach can be also used to recover F and M_c from given δv and δv_x. It is found that for a suitably chosen moment center L_c, the moment $M_c = F(L - L_c)$ is simply a linear function of either δv or δv_x. This is a reduced case where δv is proportional to δv_x. In this case, the moment M_c is given by a simple proportional relation

$$M_c = F(L - L_c) = \alpha(\delta v) \tag{11}$$

where α is a proportional constant determined by calibration. The best moment center $x = L_c$ can be determined by an optimization scheme to maximize the linearity of Eq. (11). In addition, an empirical relation between F and δv is

$$\delta v = \left[\beta_0 + \beta_1(L - L_c) + \beta_2(L - L_c)^2\right] F \tag{12}$$

where β_0, β_1, and β_2 are constants determined in calibration. Eliminating $(L - L_c)$ in Eqs. (11) and (12), one obtains a quadratic algebraic equation for F:

$$\beta_0 F^2 + (\beta_1 M_c - \delta v)F + \beta_2 M_c^2 = 0 \tag{13}$$

In principle, F and M_c can be obtained from Eqs. (11) and (13) for a given δv. However, Eq. (13) has two real roots that are often close to each other. It is not always easy to determine the correct solution without a good initial guess of F. This is a shortcoming of the simple model approach.

B. Method Based on Global Beam Deformation Profile

From Eq. (3), one knows that the displacement δv along the beam axis can be described by the theoretical relation

$$\delta v(x) = ax^2 + bx^3 \tag{14}$$

where x is the coordinate along the beam axis, δv is obtained using Eq. (8), and the coefficients a and b are related to F and M_c. In reality, however, the relation between (a and b) and (F and M_c) is not as simple as that given by Eq. (3). The empirical relations are symbolically expressed as

$$F = f_1(a, b), \qquad M_c = f_2(a, b) \tag{15}$$

For a given data point (a, b), a local second-order polynomial fit to a group of neighboring calibration data points is used to recover F

and M_c. As an alternative, we also use a simple model approach to calculate F and M_c. The empirical functional relations are

$$a = \left[a_0 + a_1(L - L_c) + a_2(L - L_c)^2\right]F$$
$$b = \left[b_0 + b_1(L - L_c) + b_2(L - L_c)^2\right]F \tag{16}$$

where (a_0, a_1, a_2) and (b_0, b_1, b_2) are determined in calibration. The solution to Eq. (16) is

$$L - L_c = \left(-c_1 \pm \sqrt{c_1^2 - 4c_2c_0}\right)\Big/(2c_2)$$
$$F = a\Big/\left[a_0 + a_1(L - L_c) + a_2(L - L_c)^2\right] \tag{17}$$

where $c_0 = b_0a/b - a_0$, $c_1 = b_1a/b - a_1$, and $c_2 = b_2a/b - a_2$.

C. Uncertainty

For uncertainty analysis, consider the general functional relations between F and M_c and δv and δv_x,

$$F = f_1(\delta v, \delta v_x, \boldsymbol{p}), \qquad M_c = f_2(\delta v, \delta v_x, \boldsymbol{q}) \tag{18}$$

where $\boldsymbol{p} = [p_1, p_2, \ldots, p_N]$ and $\boldsymbol{q} = [q_1, q_2, \ldots, q_N]$ are the parameters characterizing the functional relations. A standard uncertainty analysis[6] gives the error propagation equations for the relative variances of F and M_c,

$$\frac{\text{var}(F)}{F^2} = \sum_{i=1}^{N} S_{1p_i}^2 \frac{\text{var}(p_i)}{p_i^2} + S_{1\delta v}^2 \frac{\text{var}(\delta v)}{(\delta v)^2} + S_{1\delta v_x}^2 \frac{\text{var}(\delta v_x)}{(\delta v_x)^2}$$
$$+ S_{1\delta v}S_{1\delta v_x} R(\delta v, \delta v_x) \frac{[\text{var}(\delta v)\,\text{var}(\delta v_x)]^{\frac{1}{2}}}{\delta v \delta v_x} + \frac{\text{var}(F)_{\text{DR}}}{F^2} \tag{19}$$

$$\frac{\text{var}(M_c)}{M_c^2} = \sum_{i=1}^{N} S_{2q_i}^2 \frac{\text{var}(q_i)}{q_i^2} + S_{2\delta v}^2 \frac{\text{var}(\delta v)}{(\delta v)^2} + S_{2\delta v_x}^2 \frac{\text{var}(\delta v_x)}{(\delta v_x)^2}$$
$$+ S_{2\delta v}S_{2\delta v_x} R(\delta v, \delta v_x) \frac{[\text{var}(\delta v)\,\text{var}(\delta v_x)]^{\frac{1}{2}}}{\delta v \delta v_x} + \frac{\text{var}(M_c)_{\text{DR}}}{M_c^2} \tag{20}$$

where the sensitivity coefficients are $S_{1p_i} = (p_i/F)(\partial F/\partial p_i)$, $S_{2q_i} = (q_i/M_c)(\partial M_c/\partial q_i)$, $S_{1\delta v} = (\delta v/F)(\partial F/\partial \delta v)$, $S_{1\delta v_x} = (\delta v_x/F)(\partial F/\partial \delta v_x)$, $S_{2\delta v} = (\delta v/M_c)(\partial M_c/\partial \delta v)$, and $S_{2\delta v_x} = (\delta v_x/M_c)(\partial M_c/\partial \delta v_x)$. The correlation coefficient $R(\zeta_i, \zeta_j)$ between the variables ζ_i and ζ_j is defined as $R(\zeta_i, \zeta_j) = \text{cov}(\zeta_i\zeta_j)/[\text{var}(\zeta_i)\,\text{var}(\zeta_j)]^{1/2}$, and the variance and covariance are $\text{var}(\zeta_i) = \langle \Delta\zeta_i^2 \rangle$ and $\text{cov}(\zeta_i\zeta_j) = \langle \Delta\zeta_i \Delta\zeta_j \rangle$, where the $\langle\ \rangle$ denotes the statistical ensemble average and $\Delta\zeta_i = \zeta_i - \langle\zeta_i\rangle$ is the variation. There are two types of contributions to the total uncertainties in F and M_c. The summation terms in the right-hand side of Eqs. (19) and (20) are the uncertainties in least-squares estimation of the coefficients $\boldsymbol{p}$ and $\boldsymbol{q}$ in the data reduction models. The other three terms in the right-hand side are the uncertainties in measurements of δv and δv_x. The uncertainties in measurements of δv and δv_x are determined by the accuracy of the camera calibration. (The relative error is about 1/60,000 for the videogrammetric system used.) In addition, $\text{var}(F)_{\text{DR}}/F^2$ and $\text{var}(M_c)_{\text{DR}}/M_c^2$ are important bias errors associated with the mathematical data reduction models that fail to describe accurately the behavior of measurement data. These errors will be further discussed to compare the optical method with strain gauge balances.

The correlation terms of Eqs. (19) and (20) are more intriguing because they could be positive or negative. The total uncertainties decrease when the correlation terms are negative, and otherwise the total uncertainties increase. Based on the linear theoretical relation (4), the correlation between δv and δv_x can be calculated, that is,

$$\langle \Delta(\delta v)\Delta(\delta v_x)\rangle = \frac{x^3\langle(\Delta F)^2\rangle}{12(EI)^2}[x - 2(L - L_c)][x - 3(L - L_c)] \tag{21}$$

The correlation terms in Eqs. (19) and (20) are

$$S_{1\delta v}S_{1\delta v_x}\frac{\langle \Delta(\delta v)\Delta(\delta v_x)\rangle}{\delta v \delta v_x} = \frac{\langle(\Delta F)^2\rangle}{x^2F^2}[x - 2(L - L_c)][x - 3(L - L_c)]$$
$$S_{2\delta v}S_{2\delta v_x}\frac{\langle \Delta(\delta v)\Delta(\delta v_x)\rangle}{\delta v \delta v_x} = \frac{\langle(\Delta F)^2\rangle}{6M_c^2}[x - 2(L - L_c)][x - 3(L - L_c)] \tag{22}$$

The correlation terms are negative for $2(L - L_c) < x < 3(L - L_c)$ and $0 < L_c < L$. Furthermore, at a fixed target location $x = rL$ ($r \le 1$ is a fractional constant), the correlation terms are negative when the moment center $x = L_c$ is in $(2 - r)L/2 < L_c < (3 - r)L/3$. This analysis indicates that the moment center can be suitably selected to reduce the total uncertainties in measurements.

IV. Videogrammetric System

In this study, elastic deformation of a beam is measured using a videogrammetric system. Based on the principles of close-range photogrammetry, the videogrammetric system measures the coordinates of targets distributed along the beam from target centroids in digital images. Deformation of the beam is then calculated from the measured target coordinates. Figure 3 shows a schematic of a two-camera videogrammetric system used for deformation measurements. The basic hardware for this system consists of two Hitachi KP-F1 charge-coupled device cameras and a Dell personal computer with a Matrox Pulsar frame grabber board. Lenses with different focal lengths can be selected, depending on a ratio between the object size and the distance of the object from the cameras. In the tests reported in this paper, two 15-mm lenses were used. The cameras with different lenses can be rapidly calibrated with a good accuracy with an optimization camera method.[7] Ordinary light sources can be used as long as they can provide sufficiently high contrast of targets. For retroreflecting targets, light sources should be placed near the cameras to achieve the maximum reflection from the targets. In the beam tests, an array of retroreflecting targets were placed on a beam. Software includes programs for image acquisition, target tracking/centroid calculations, and camera calibration. This system is able to provide three-dimensional coordinates X, Y, and Z in almost real time. The accuracy of the videogrammetric system used for this work is typically 1/60,000, which is a ratio between the metric measurement error on the object and the distance of the cameras from the object. After the coordinates of the targets on the beam are obtained, the deformation $(\delta v, \delta v_x)$ can be calculated. The data reduction programs for calculating the deformation,

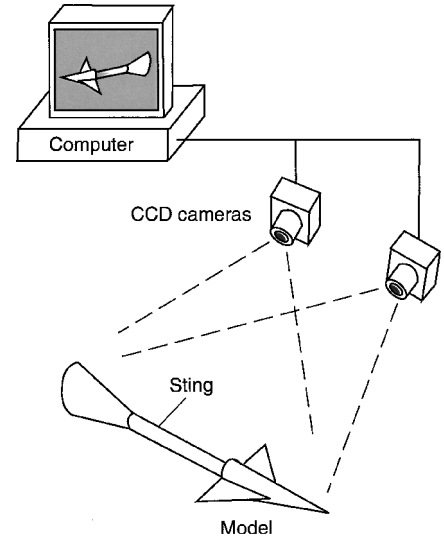

Fig. 3 Two-camera videogrammetric system for deformation measurements in wind tunnels.

force, and moment are written in MATLAB®. The technical aspects of the videogrammetric system have been described in detail by Liu et al.[7,8] Comprehensive reviews of the application of videogrammetry to wind-tunnel testing have been given by Burner and Liu[2] and Liu et al.[7]

V. Experimental Results

A. Simple Beams

Three simple beams have been calibrated to examine the proposed methodology of recovering the normal force and pitching moment. One is a brass beam with a 0.75×0.75 in. (19.1×19.1 mm) square cross section and the rigidity of $EI = 350 \times 10^3$ lb-in.^{2} (102.4 kg-m^2). Another is a more flexible stainless-steel beam that is actually a flat plate with a rectangular cross section of 1.5×0.25 in. (38.1×6.35 mm) and the rigidity of $EI = 47 \times 10^3$ lb-in.^{2} (13.8 kg-m^2). The third is a more rigid stainless-steel beam having a circular cross section with a diameter 0.75 in. (19.1 mm) and the rigidity of $EI = 442 \times 10^3$ lb-in.^{2} (129.3 kg-m^2). A number of retroreflecting targets are placed along the centerline of each beam for deformation measurements.

Figure 4 shows the local displacement and slope change δv and δv_x as a function of the normal force for the brass beam at four different loading positions $L = 20.52$, 21.86, 23.17, and 24.58 in. (0.521, 0.555, 0.588, and 0.624 m). It has been found that the dependence of both the local displacement and the slope change on the pitching moment is linear when the moment center is suitably chosen. The linear relations are clearly shown in Fig. 5 for the brass beam, where the moment center determined by an optimization scheme is located at $L_c = 9.03$ in (0.229 m). This linearity is utilized in the simple model method for data reduction. Figure 6 shows the errors in measurements of the normal force and pitching moment by using the method based on local displacement and slope change for the brass beam. The local second-order polynomial and the simple model methods are used for data interpolation. For the soft and stiff stainless steel beams, Fig. 7 shows the measurement errors in the normal force and pitching moment. Typically, the relative errors in the normal force and pitching moment are roughly within ± 10 and $\pm 5\%$ in the calibration ranges, respectively.

The method based on global deformation profile is used to recover the normal force and pitching moment for the brass beam. Figure 8 shows measured deformation profiles of the brass beam for different loads at the loading position $L = 24.58$ in. (0.624 m).

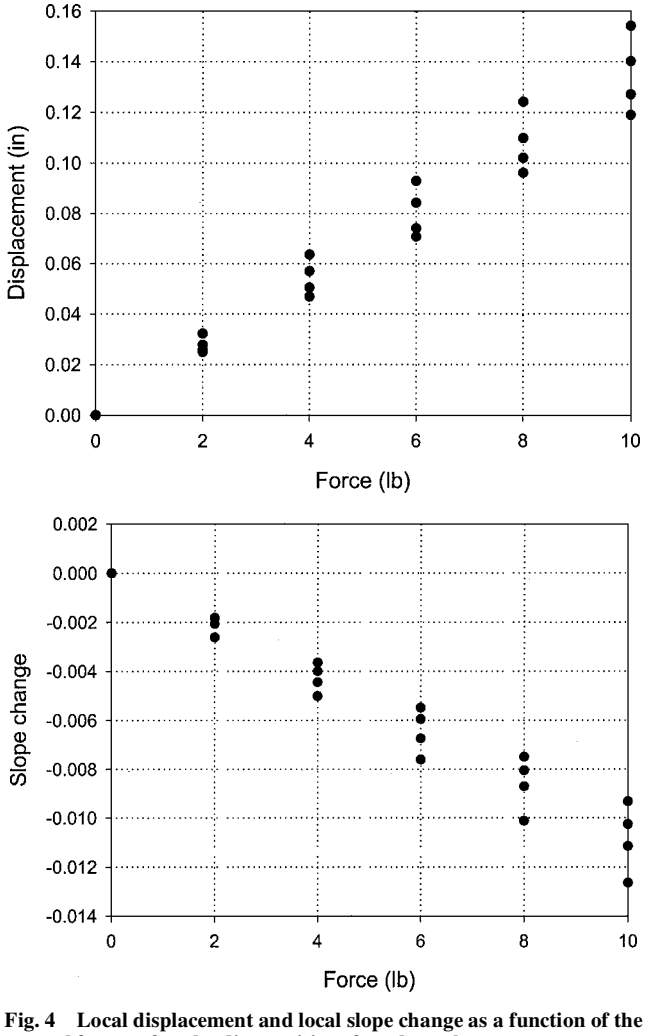

Fig. 4 Local displacement and local slope change as a function of the normal force at four loading positions for a brass beam.

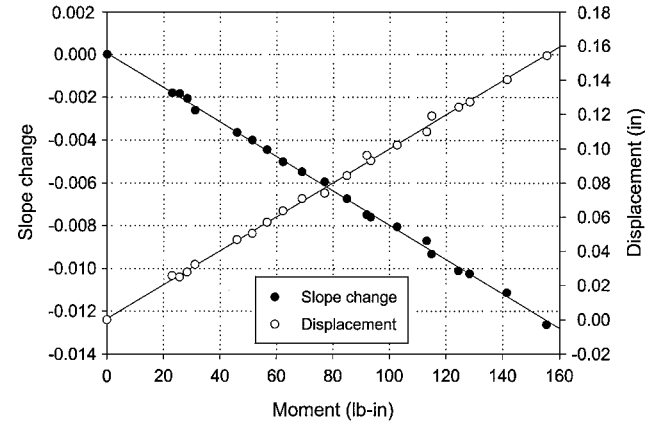

Fig. 5 Local displacement and slope change as a function of the pitching moment for a brass beam.

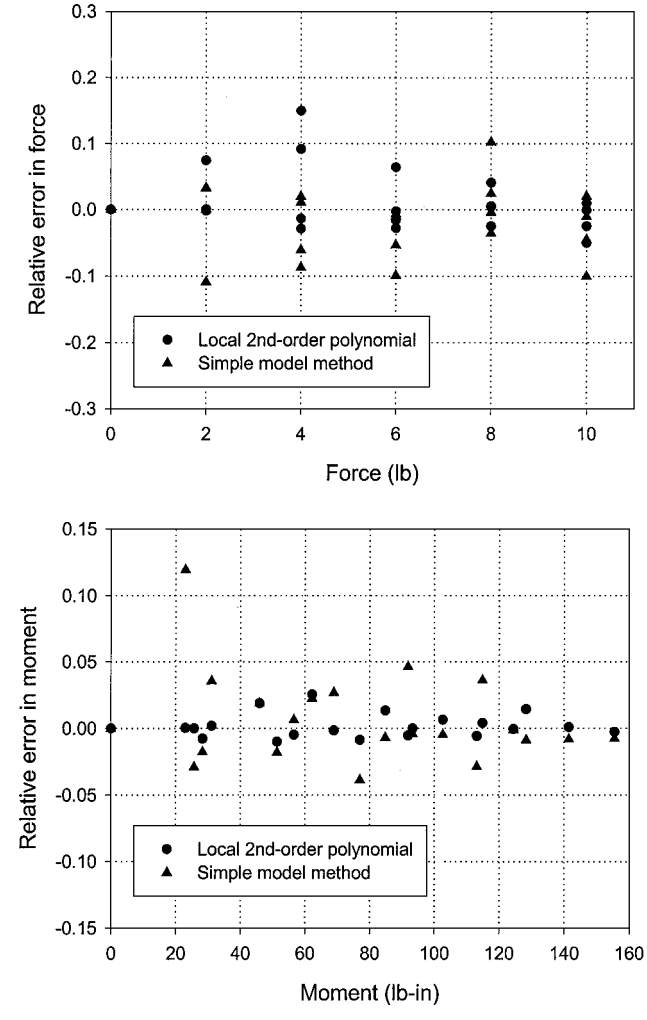

Fig. 6 Relative errors in the normal force and pitching moment for a brass beam when the data reduction method is based on local displacement and slope change.

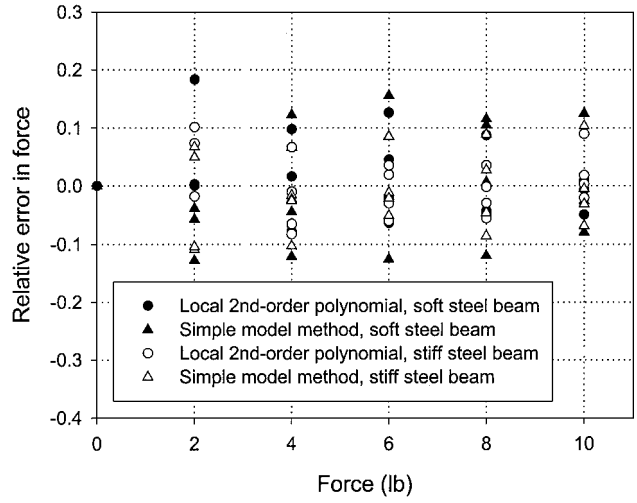

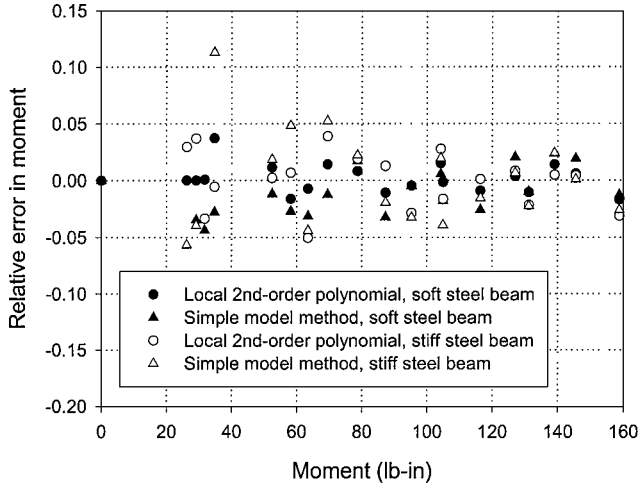

Fig. 7 Relative errors in the normal force and pitching moment for a soft steel beam and a stiff steel beam when data reduction method is based on the local displacement and slope change.

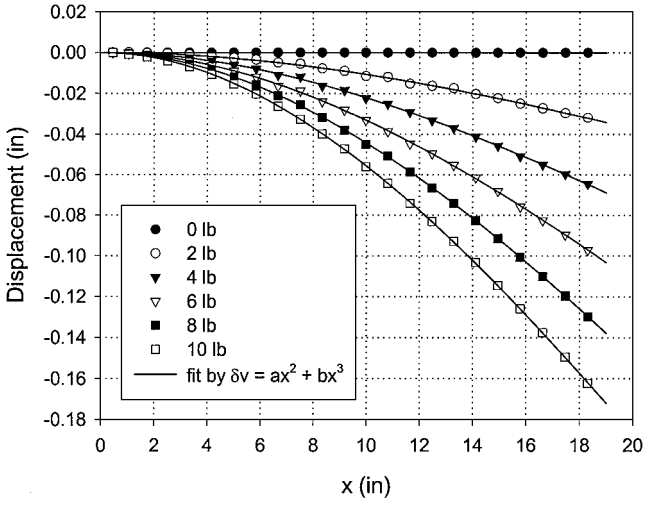

Fig. 8 Measured deformation profiles of a brass beam and the fit by $\delta v(x) = ax^2 + bx^3$ at the loading position $L = 24.58$ in. (0.624 m).

These measured data can be well fitted by the theoretical solution $\delta v(x) = ax^2 + bx^3$. The errors in measurements of the normal force and pitching moment are shown in Fig. 9, where the local second-order polynomial and simple model methods are used for data interpolation. Compared to the method based on the local displacement and slope change, the method based on the global deformation profile gives smaller relative errors in the normal force (within ±5%) and pitching moment (within ±3%) for the brass beam.

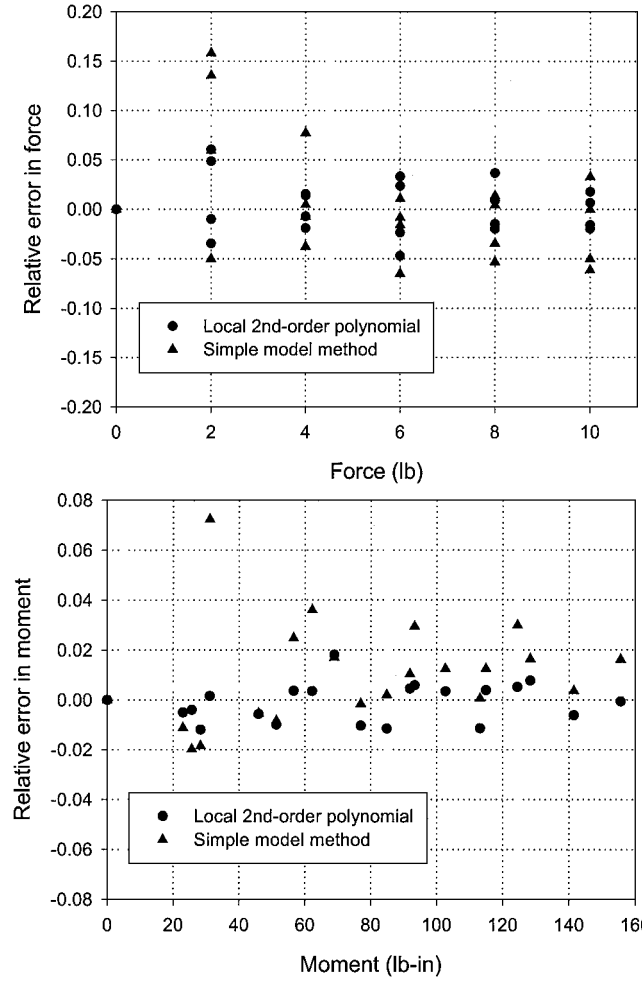

Fig. 9 Relative errors in the normal force and pitching moment for a brass beam when the data reduction method is based on the global deformation profile.

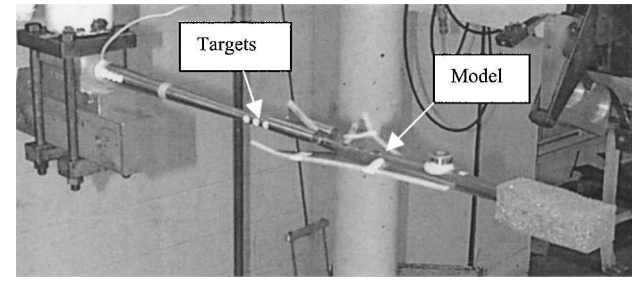

Fig. 10 Sting–model configuration with targets.

B. Sting–Model Combination

A steel sting–model combination used in the Unitary Tunnel at NASA Langley Research Center was calibrated, as shown in Fig. 10. The sting has a tapering circular cross section with a linearly decreasing radius from 0.5975 to 0.197 in. (15.2 to 5 mm). Accordingly, the rigidity of the sting decreases from 2800×10^3 to 38×10^3 lb-in.^{2} (819.4 to 11.1 kg-m^2) and the mean rigidity is 930×10^3 lb-in.^{2} (272.1 kg-m^2). In calibration tests, the maximum displacement of the sting is about 0.03 in. (0.76 mm), and the maximum change of the local bending angle is about 0.23 deg. Two strain gauge bridges were also installed on the sting for measurement of the normal force and pitching moment, which allows a direct comparison between the strain gauge method and the optical method.

During calibration tests, a number of dead weights from 2 to 10 lb (0.91 to 4.54 kg) were loaded at three different locations on the model to generate the required forces and moments. Three retroreflecting targets were placed near the model for measuring local deformation, and four other targets were placed near the support

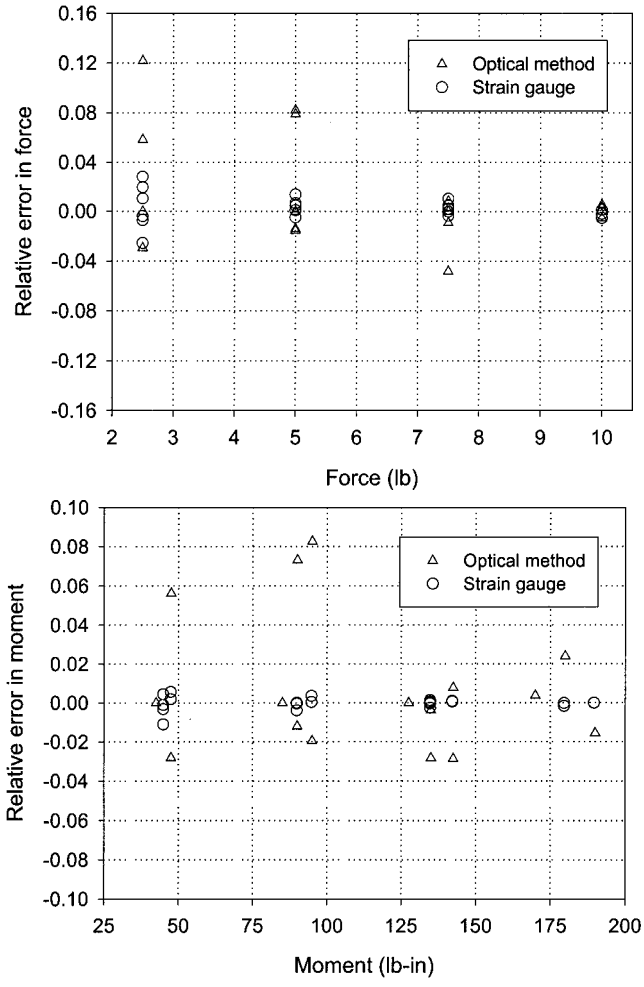

Fig. 11 Comparison between optical method and strain gauges in measurements of normal force and pitching moment for the steel sting–model configuration; optical method based on the local displacement and slope change.

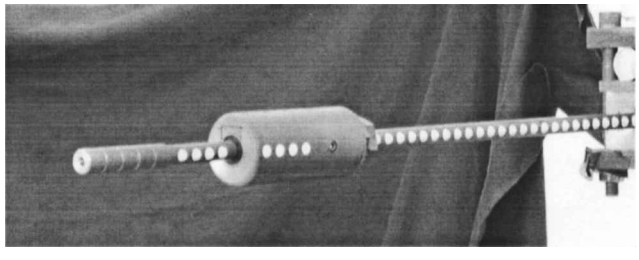

Fig. 12 Three-force beam with targets.

as a reference. The local deformation quantities δv and δv_x were measured using the videogrammetric system. The method based on the local displacement and slope change was used to determine the normal force and pitching moment. Figure 11 shows the measurement errors in the normal force and pitching moment for this steel sting–model combination. The results indicate that the optical method based on remote deformation measurement is less accurate than the more sensitive strain gauges. The relative errors in the normal force and pitching moment obtained by the optical method are about $\pm 5\%$ in comparison with $\pm 2\%$ given by the strain gauges.

C. Three-Force Beam

To measure the axial force along with the normal force and pitching moment, a three-force beam has been designed and fabricated. As shown in Fig. 12, the three-force beam consists of a simple beam and a spring/bearing device that only allows translational motion along the beam axis. The structure of the spring/bearing device is shown in Fig. 13. A steel axial load shaft (made of medium-alloy A-2 steel) is a moving rod that is constrained by a linear bearing mounted inside the hardware assembly. The rod is hardened and has a ground surface finish of 0.625 (+0.0002/−0.0000) in. (15.87 mm) on the diameter. This tight tolerance provides a very close interfaced fit with the bearing so that all lateral movement is minimized. Another main component of the device is the spring that balances the applied axial force. Ranges of the springs with different spring constants are available that can be selected to meet the requirements of the axial force calibration. The three-force beam attaches to the extended end of a 0.625-in. (15.87-mm)-diam stainless-steel beam. The spring/bearing device housing has an outside diameter of 2.38 in. (60.5 mm) and is 6.0 in. (152.4 mm) long. The extended length of the entire beam assembly is 28.25 in. (0.718 m) in the balance calibration apparatus. As shown in Fig. 12, a number of retroreflecting targets are placed on the simple beam for measuring the beam deformation. Four targets are placed on the spring/bearing device as a reference, and another four targets are placed on the movable shaft for measuring the axial translational motion relative to the reference targets. The average spacing between retroreflective targets is approximately 0.65 in. (16.5 mm).

The normal force and pitching moment are obtained with the same methods as earlier described. The measurement errors in the normal force and pitching moment are shown in Fig. 14, indicating $\pm 4\%$ errors for the normal force and $\pm 3\%$ errors for the pitching moment. The axial force F_{ax} is related to the axial displacement δx by a linear relation $F_{ax} - F_{ax0} = k\delta x$, where k is an effective spring coefficient and F_{ax0} is the force at $\delta x = 0$. When the normal force F_N and pitching moment M_c act on the beam, k and F_{ax0} are not true constants, which are weakly dependent on F_N and M_c due to the presence of friction in the bearing. Experiments show that k and F_{ax0} are mainly related to the loading position M_c/F_N over a certain range of the normal force. Thus, an empirical calibration relation for the axial force is $F_{ax} = k(M_c/F_N)\delta x + F_{ax0}(M_c/F_N)$, where $k(M_c/F_N)$ and $F_{ax0}(M_c/F_N)$ are empirically expressed by polynomials. Figure 15 shows the linear relation between the axial force and the measured axial displacement. Figure 16 shows the measurement errors in the axial force to be within $\pm 8\%$.

D. Further Discussion on Errors

Experiments show that the optical technique is, at this stage, less accurate than conventional strain gauge balances used in wind-tunnel testing for many years. Basic uncertainty analysis is needed to compare the optical method and strain gauge balances. Tripp and Tcheng[9] gave a general statistical analysis of measurement uncertainties of multicomponent wind-tunnel balances. According to their results, a least-square estimate of the coefficients of a multivariate second-order polynomial for calibration data showed the relative errors of 0.15% of the full-scale load in normal force. When the experimental accuracy of strain gauge balances used at NASA Langley Research Center was studied, Ferris[10] reported that the relative errors in the six force and moment components are less than 0.2% of the full-scale load. However, there is still a lack of a complete and systematic uncertainty analysis for strain gauge balances, which takes all of the elemental error sources of balance hardware units into account. Clearly, a complete uncertainty analysis requires a full set of mathematical models for all of the balance system elements. Here, instead of carrying out a complete uncertainty analysis, we give basic estimates to explain why the current optical method has much larger errors than strain gauge balances. In principle, the general uncertainty analysis formulations of Eqs. (19) and (20) are also valid for strain gauge balances as long as the local displacement δv and slope change δv_x are replaced by local strain gauge bridge outputs. Thus, we are able to rationally compare the measurement errors of δv and δv_x with those of strain gauge bridge outputs. In our experiments, the cameras are about 120 in. (about 3 m) away from the tested beams, and thus the metric resolution of the videogrammetric system is about 0.002 in. (0.05 mm) because the accuracy of the system is 1/60,000 of the distance from the object. For a typical beam, such as the brass beam whose deformation is about 0.02–0.16 in. (0.5–4.1 mm), the relative error in displacement measured by the videogrammetric system ranges from 1 to 10%. By comparison, the measurement error of a typical strain gauge bridge

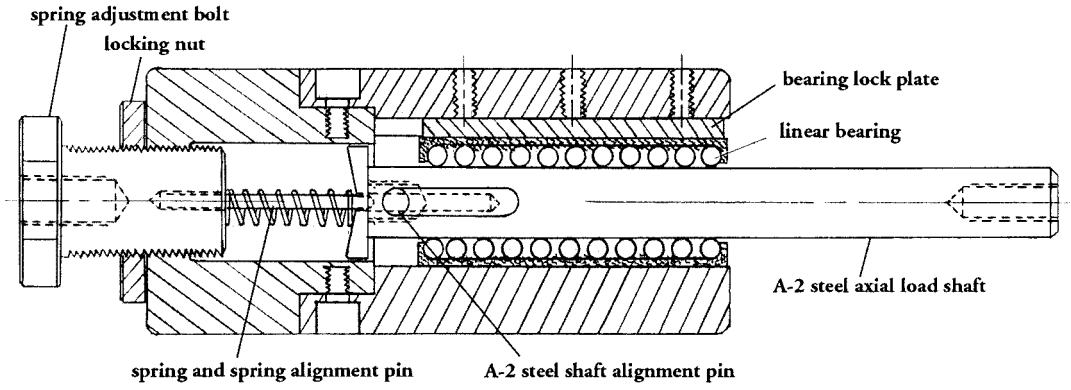

Fig. 13 Structure of the spring/bearing device.

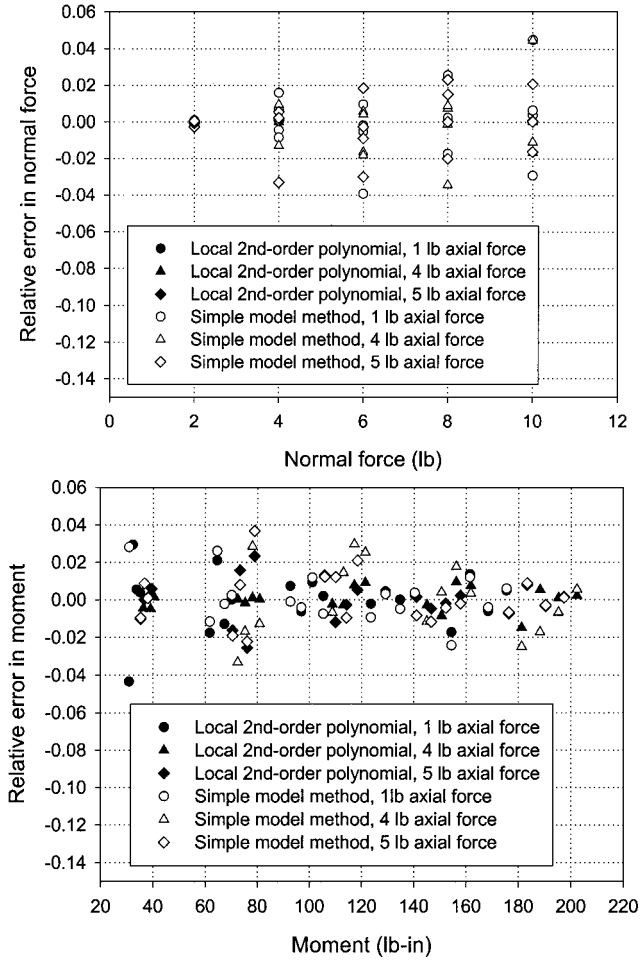

Fig. 14 Relative errors in the normal force and pitching moment for the three-force beam at different axial loads; data reduction method based on the local displacement and slope change.

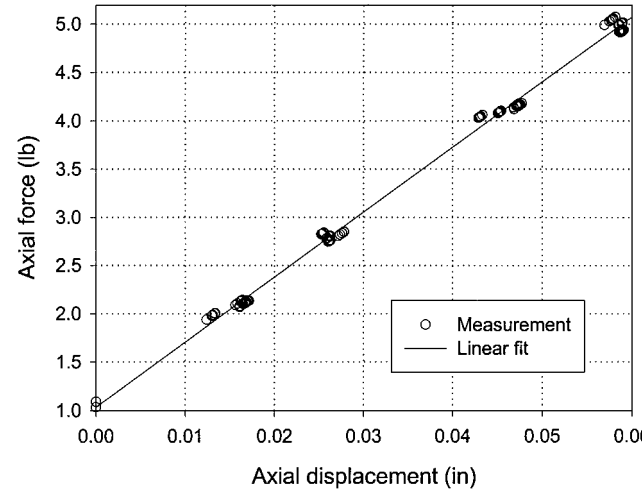

Fig. 15 Axial force as a function of the axial displacement.

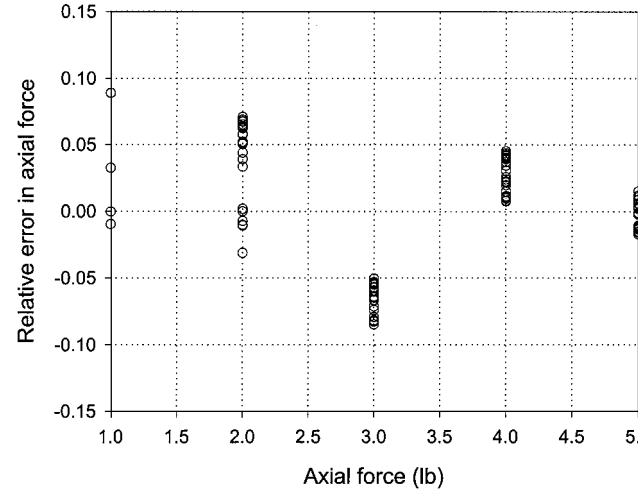

Fig. 16 Measurement errors in the axial force for the three-force beam at different normal forces and loading positions.

is typically 0.1%. In general, the videogrammetric system has a much larger measurement error than strain gauge bridges, especially when the cameras are located far from the beam. As discussed in Sec. III.C, another important error is associated with fitting the calibration data with a mathematical data reduction model. Because the structure of a strain gauge balance is deliberately designed to decouple interactions among different measurement components, forces and moment data are distributed as spreading surfaces in the parametric space. Hence, they can be reasonably described by a global second- or third-order polynomial of strain gauge bridge outputs. In contrast, the optical method based on beam deformation measurements cannot take the advantage of a specially designed structure for decoupling the different components. As a result, the measurement quantities in the optical method, such as δv and δv_x, are highly correlated. Geometrically, the normal force and pitching moment are represented by narrow conical surfaces in the parametric space of δv and δv_x. In a limiting case $\delta v \propto \delta v_x$, the narrow conical surface is reduced to a space curve. Because these narrow conical surfaces cannot be accurately fitted by a global second or third polynomial, the current optical method has a larger error in fitting calibration data than a strain gauge balance. This error associated with data reduction model dominates the total uncertainty of the optical method presented in this work. Therefore, a more reasonable mathematical model for data reduction is desirable to describe accurately the narrow conical surface in the parametric space and to reduce the measurement uncertainty.

VI. Conclusions

The methodology of optically measuring aerodynamic loads has been developed based on beam deformation theory. A two-camera videogrammetric system was used for optical deformation measurements. The data reduction models for extracting the normal force and pitching moment utilized either the local displacement and slope change or the global beam deformation profile. Calibration data interpolation was made by either the local second-order polynomial fit or the simple model approach. To validate the proposed methodology, three simple metallic beams with different rigidities were tested to recover the normal force and pitching moment. A steel sting–model combination was also calibrated for a direct comparison between the strain gauge method and optical method. Typically, the relative errors in the normal force and pitching moment range from ± 5 to $\pm 10\%$ and ± 2 to $\pm 5\%$, respectively. To determine the axial force, a three-force beam that allows the axial translational motion was designed and fabricated. The axial force was obtained by measuring the translational motion of a movable shaft in a spring/bearing device. The measurement errors in the axial force are within $\pm 8\%$. To date, the current optical method is much less accurate than well-developed strain gauge balances (typically 0.15%) due to less accurate remote optical metric measurements and a poor polynomial fitting for highly correlated quantities in the parametric space. At this stage, the optical method is useful as an alternative in certain cases where strain gauge balances cannot be easily applied and in some preliminary tests that do not require a high accuracy. In addition, the optical method can be integrated with other modern optical techniques for wind-tunnel testing, such as videogrammetric model attitude/deformation measurement, pressure- and temperature-sensitive paints, and particle image velocimetry. Further research efforts will be made to improve the accuracy of the optical method in measuring aerodynamic loads.

References

[1]Tripp, J. S., and Tcheng, P., "Proceeding of First International Symposium on Strain Gauge Balances," NASA Langley Research Center, Hampton, VA, March 1999.

[2]Burner, A. W., and Liu, T., "Videogrammetric Model Deformation Measurement Technique," *Journal of Aircraft*, Vol. 38, No. 4, 2001, pp. 745–754.

[3]Burner, A. W., "Model Deformation Measurements at NASA Langley Research Center," *Advanced Aerodynamic Measurement Technology*, CP-601, AGARD, 1997, pp. 34-1–34-9.

[4]Bisplinghoff, R., Mar, J. W., and Pian, T. H. H., *Statics of Deformable Solids*, Addison–Wesley, New York, 1965, Chap. 7.

[5]Timoshenko, S., and Goodier, J. N., *Theory of Elasticity*, McGraw–Hill, New York, 1970, Chap. 3.

[6]Bevington, P. R., and Robinson, D. K., *Data Reduction and Error Analysis for the Physical Sciences*, 2nd ed., McGraw–Hill, New York, 1992, Chap. 3.

[7]Liu, T., Cattafesta, L. N., III, Radeztsky, R. H., and Burner, A. W., "Photogrammetry Applied to Wind-Tunnel Testing," *AIAA Journal*, Vol. 38, No. 6, 2000, pp. 964–971.

[8]Liu, T., Radeztsky, R., Garg, S., and Cattafesta, L., "A Videogrammetric Model Deformation System and Its Integration with Pressure Paint," AIAA Paper 99-0568, 1999.

[9]Tripp, L., and Tcheng, P., "Determination of Measurement Uncertainties of Multi-Component Wind Tunnel Balances," AIAA Paper 94-2589, 1994.

[10]Ferris, A. T., "An Improved Method for Determining Force Balance Calibration Accuracy," Instrument Society of America, ISA Paper 93-092, May 1993.

W. R. Lempert
Guest Associate Editor